Available online at www.sciencedirect.com
SCIENCE DIRECT®
Combustion and Flame 137 (2004) 198–221
Combustion and Flame
www.elsevier.com/locate/jnlabr/cnf

Extinction criterion for unsteady, opposing-jet diffusion flames

V.R. Katta,[a,*] T.R. Meyer,[a] M.S. Brown,[a] J.R. Gord,[b] and W.M. Roquemore [b]

[a] *Innovative Scientific Solutions, Inc., 2766 Indian Ripple Road, Dayton, OH 45440, USA*
[b] *Air Force Research Laboratory, Propulsion Directorate, Wright–Patterson Air Force Base, OH 45433, USA*

Received 25 April 2003; received in revised form 29 January 2004; accepted 9 February 2004

Abstract

Dynamic flames are known to survive at strain rates that are much higher than those associated with steady-state flames. A numerical and experimental investigation is performed to aid the understanding of the extinction process associated with unsteady flames. Spatially locked unsteady flames in an opposing-jet-flow burner are established and stretched by simultaneously driving one vortex from the air side and another from the fuel side. Changes in the structure of the flame during its interaction with the incoming vortices and with the instability-generated secondary vortices are investigated using a time-dependent computational-fluid-dynamics-with-chemistry (CFDC) code known as UNICORN (UNsteady Ignition and COmbustion with ReactioNs). The combustion process is simulated using a detailed-chemical-kinetics model that incorporates 13 species and 74 reactions. Slow-moving vortices produce a wrinkled but continuous flame, while fast-moving vortices create a locally quenched flame with its edge wrapped around the merged vortical structures. In an attempt to characterize the observed quenching process, five variables—namely, air-side, fuel-side, and stoichiometric strain rates and maximum and stoichiometric scalar dissipation rates—are investigated. It is found that these characteristic parameters cannot be used to describe the quenching process associated with unsteady flames. The flow and chemical nonequilibrium states associated with the unsteady flames are responsible for changes in the extinction values of these traditional characteristic variables. However, even though the quenching values of the scalar dissipation rates increase with the velocity of the incoming vortices, the variations are much smaller than those observed in the strain rates. It is proposed that a variable that is proportional to the air-side strain rate and inversely proportional to the rate of change in the flame temperature can be used to characterize the unsteady quenching process uniquely.

Keywords: Extinction; Unsteady flames; Turbulent flames; Diffusion flames; Vortex–flame interaction; Nonequilibrium flows

1. Introduction

Studies of the structure of unsteady flames are important for gaining an understanding of fundamental combustion processes. Such studies provide insight into turbulent-combustion phenomena and aid the development and evaluation of simplified models that can be used in design codes for practical combustion systems. Unsteady flames associated with turbulent combustion are subjected to stretching that varies with time; typically, the time scale for the changes in strain rate is comparable to those of the chemical (e.g., reaction time) and physical (e.g., diffusion time) responses of the system. Because of the resulting nonequilibrium environment, the structure of a stretched unsteady flame differs from that of a stretched steady-state flame.

* Corresponding author.
E-mail address: vrkatta@erinet.com (V.R. Katta).

0010-2180/$ – see front matter
doi:10.1016/j.combustflame.2004.02.004

Numerous experimental and numerical investigations [1–3] have been performed to quantify the scalar structure of steady-state, aerodynamically strained, planar, counterflow diffusion flames. Such studies have not only provided benchmark experimental data but also yielded valuable insight into the steady-state behavior of the planar flame that is subjected to stretch (or strain) rates up to the extinction limits. In practical combustion devices, flames are subjected to severe unsteadiness that results from the random motion of the vortices [4,5]. To retain the analytical and experimental simplicity offered by planar diffusion flames, however, the unsteady flame structure is also investigated in counterflow flames by fluctuating the fuel and air jets simultaneously and sinusoidally [6–8]. Although the results have indicated that unsteady flames can be stretched beyond the steady-state extinction limit [9], these studies are mainly focused on understanding the behavior of the flame when subjected to moderate-amplitude fluctuations in strain rate [7], reactant composition [7,10], and partial premixing [11]. Since the extinction strain rate, in general, is higher than the maximum strain rate at which ignition can occur, temporal flame extinction at any time within the fluctuation cycle in a periodically oscillating counterflow flame could lead to complete flame extinction. Consequently, strain rates that are lower than the extinction limit are often used in the periodically oscillating-flame experiments.

Using numerical simulations Ghoniem et al. [12] have demonstrated that partial extinction and reignition can occur in a periodically oscillating counterflow flame when it is subjected to a high-amplitude, high-frequency perturbation. Recently, Egolfopoulos [13] provided a detailed analysis of unsteady counterflow flames and concluded that even though the flame response to strain-rate perturbations diminishes at higher frequencies, the substantial transient effects that still exist in the flame zone lead to partial extinction and reignition. Following these findings, Cuenot et al. [14] proposed the following extinction criterion: for an unsteady flame to be extinguished, the applied strain rate should not only exceed the critical steady-state extinction value but also remain higher over a characteristic time.

The unsteady extinction criterion proposed by Cuenot et al. [14] uses global quantities such as applied strain rate, crossover temperature, and characteristic time, which are readily available for periodically oscillating-counterflow-flame configurations. However, in the case of flames stretched by vortices, such global quantities cannot easily be estimated since the local strain rate and characteristic-time scale strongly depend on the evolution of the vortex (note that entrainment modifies the vortex-propagation velocity) in the given flowfield. Therefore, an unsteady extinction criterion based on local quantities is also required for the prediction of extinction during a vortex/flame interaction process.

During vortex/flame interactions, which are often considered to be the building blocks of statistical theories of turbulence, the flame surface is subjected not only to unsteadiness but also to deformation. To investigate the effects of curvature on unsteady flames, both theoretical and experimental studies have been initiated [15–18]. In particular, experiments designed by Roberts et al. [19] and by Rolon et al. [20] have generated considerable interest, especially because of their unique ability to inject a well-characterized vortex toward the flame surface. Numerous investigations have been performed by varying the size and strength of the vortex in opposing-jet burners [20] in attempts to understand global features such as scale [21,22] and origin [23] effects and localized features such as annular-quenching [24] and non-adiabatic-equilibrium-temperature [25,26] phenomena.

Recent studies on vortex/flame interactions by Katta and Roquemore [23] revealed that the extinction strain rate of an unsteady flame is dependent on whether the flame is traveling or stationary. By issuing vortices from the fuel and air sides of an opposing-flow jet diffusion flame, they simulated traveling and stationary unsteady flames. In the traveling unsteady flame, not only the strain rate on the flame but also the flame location was changed with time; in the stationary unsteady flame, on the other hand, the strain rate was varied with time by locking its position spatially. The latter unsteady flames, established by issuing vortices simultaneously from the air and fuel sides, offered a pathway to understanding the unsteady-flame structure near extinction.

Several investigators have developed models [17, 27,28] for the study of the interaction between a planar flame and an induced vortex. In all of these models, it was assumed that an artificially created (by specifying the vorticity field) vortex pair interacts with a flat flame formed in a parallel flow. Although this assumption has advantages in exploring interesting aspects of vortex/flame interactions, investigations employing these synthesized vortices do not represent actual interactions in opposing-jet flames and, hence, cannot facilitate direct comparisons between predictions and measurements, making verification of the former very difficult.

Recent advances in computer hardware and the need to improve the understanding of combustion phenomena under complex practical situations have led to the development of two- and three-dimensional computational-fluid-dynamics models that incorporate detailed chemical kinetics (CFDC) [29,30]. Complete simulation of the opposing-jet flame using multidimensional models not only eliminated concerns

regarding the simplified analyses but also provided a valuable tool for studying vortex/flame interactions in premixed [19,31] and diffusion [20,24] flames. In the present investigation, a well-tested CFDC model was used to understand the unsteady flame structure near extinction and to characterize the extinction process.

2. Mathematical model

A time-dependent axisymmetric model known as UNICORN (UNsteady Ignition and COmbustion with ReactioNs) [32] was used for the simulation of unsteady flames associated with an opposing-jet-flow burner. This model solves the Navier–Stokes and species- and energy-conservation equations written in the cylindrical-coordinate (z–r) system. A detailed-chemical-kinetics model is employed to describe the hydrogen–air combustion process. This model consists of 13 species—namely, H_2, O_2, H, O, OH, H_2O, HO_2, H_2O_2, N, NO, NO_2, N_2O, and N_2—and 74 elementary reactions among the constituent species. The rate constants for this H_2–O_2–N_2 reaction system were obtained from Ref. [33].

Temperature- and species-dependent property calculations are incorporated into the model. The governing equations are integrated on a nonuniform staggered-grid system. An orthogonal grid having rapidly expanding cell sizes in both the axial and the radial directions is employed. The finite-difference forms of the momentum equations are obtained using an implicit QUICKEST scheme [34,35], and those of the species and energy equations are obtained using a hybrid scheme of upwind and central differencing. At every time step, the pressure field is calculated by solving the pressure Poisson equations simultaneously and utilizing the LU (lower and upper diagonal) matrix-decomposition technique. UNICORN has been validated previously by simulating various steady and unsteady counterflow [23,24,27] and coflow [30,36] jet diffusion flames.

3. Results and discussion

3.1. Burner details

The opposing-jet-flow burner used for the investigations of unsteady-flame structures was designed by Rolon, is shown in Fig. 1, and is described in detail in Ref. [20]. A flat flame is formed between fuel and air jets having velocities of 0.69 and 0.5 m/s, respectively. The hydrogen-to-nitrogen ratio used for the fuel jet is 0.38. Unsteady flames are established by injecting vortices simultaneously from the fuel and air sides. The collision of these vortices with the flame surface, in general, imposes unsteady stretch on the flame. Such a collision involving stronger vortices may also quench the flame locally and generate multiple vortices. Studies were performed to investigate various types of vortex-collision/flame interactions by incorporating different sizes of fuel- and air-side injection tubes and varying the injection durations. Air-side vortices were generated by injecting a specified amount of air through the syringe tube (Fig. 1) and then through a 5.0-mm-diameter injection tube. On the other hand, fuel-side vortices were generated by injecting a specified amount of fuel through the syringe tube and then through either a 2.0-mm- or a 5.0-mm-diameter injection tube. Two types of interactions—namely, unsteady nonstationary and unsteady stationary—are treated in the present paper. The z–r coordinate system used for the simulation of flames associated with the Rolon burner is shown in Fig. 1. Calculations for these axisymmetric flames were made using a nonuniform 601×301 mesh system distributed over a physical domain of 40×40 mm, which yielded a mesh spacing of 0.05 mm in both the axial (z) and the radial (r) directions in the region between the two nozzles.

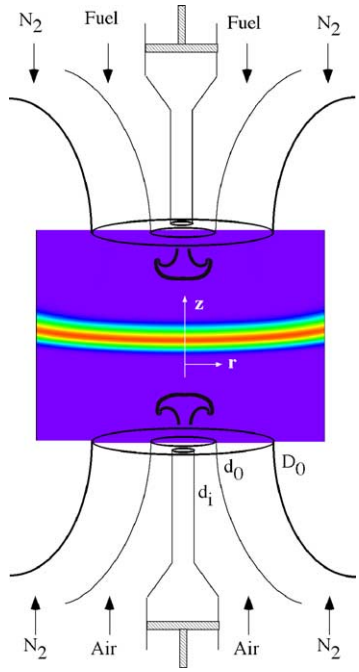

Fig. 1. Schematic diagram of the opposing-jet-flow burner used for investigations of double-vortex/flame interactions. Nitrogen-diluted hydrogen fuel and air were introduced from upper and lower nozzles, respectively. The structure of the steady-state flame is also shown in the form of the isotemperature distribution.

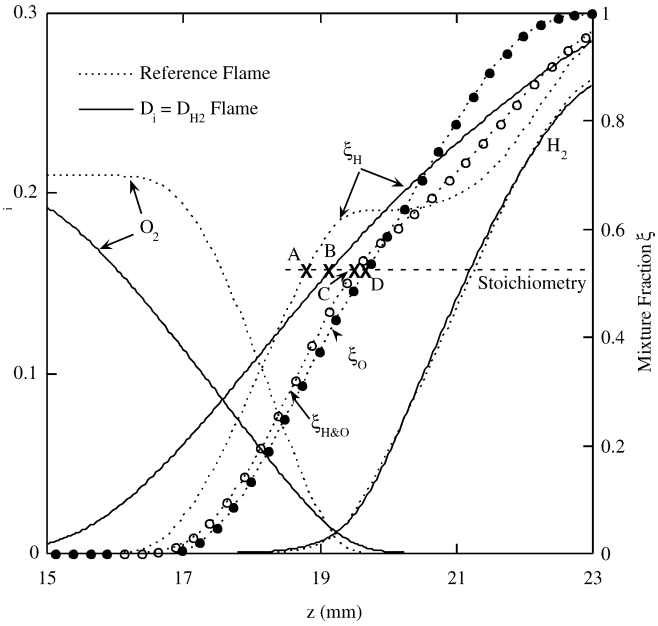

Fig. 2. Steady-state flame structures along the centerline for the reference flame (broken lines) and "$D_i = D_{H_2}$" flame (solid lines). Points A–D represent mixture fractions at stoichiometric conditions.

3.2. Steady-state flame structure

Prior to the injection of vortices, a flat flame is simulated for the experimental conditions described earlier. The computed steady-state flame in the form of isotemperature distributions is shown in Fig. 1, along with the schematic diagram of the burner. Note that the gravitation force in this simulation is neglected. The slight upward curvature of the flame surface develops as a result of the lower density of the hydrogen fuel. Apparently, the velocity difference used for the fuel and air jets (0.69 vs 0.5 m/s, respectively) did not provide a perfect balance of momentum for the two jets, resulting in a slight shift in the flame location from the burner mid-plane toward the air jet (lower nozzle). The flame structure along the centerline (also known as the stagnation line in this opposing-jet-flow configuration) is shown in Figs. 2–4 and is referred to as the reference flame. The fuel, oxygen, and mixture-fraction (ξ) distributions are represented in Fig. 2 by broken lines (reference flame). As a result of nonequilibrium chemistry, hydrogen and oxygen coexist in an overlap region that is ∼2 mm thick. Although several forms of mixture-fraction definition are available in the literature [37], no particular form has an advantage over the others in describing the flame structure, and in many studies a particular form of mixture fraction is selected over others as a matter of convenience [38]. The one used in the present study is based on the mass fraction of fluid that originates from the fuel jet at a given location [37]. In hydrogen flames this mixture fraction (ξ_H) is computed from the following equation:

$$\xi_H = \frac{w_{H_2}}{Y^0_{H_2}}\left[\left(\frac{Y_{H_2}}{w_{H_2}} + \frac{Y_{H_2O}}{w_{H_2O}} + \frac{Y_{H_2O_2}}{w_{H_2O_2}}\right) + \frac{1}{2}\left(\frac{Y_H}{w_H} + \frac{Y_{OH}}{w_{OH}} + \frac{Y_{HO_2}}{w_{HO_2}}\right)\right]. \quad (1)$$

Here, Y_i represents the mass fraction of the ith species, w_i represents the molecular weight of the ith species, and the superscript 0 represents the state in the fuel jet. The stoichiometric value of the mixture fraction (ξ_{stoich}), calculated based on the flow conditions used in this study, is 0.5264. This stoichiometric condition is established (Location A in Fig. 2) on the oxygen-rich side of the reaction zone.

Fig. 2 shows that the mixture fraction for the reference flame did not increase monotonically from zero on the air side ($z = 0$) to unity on the fuel side ($z = 40$ mm). Rather, it reached a peak value at about $z = 19.5$ mm and then stayed at a plateau before rising to unity. This nonmonotonic behavior suggests that the laminar flame shown in Fig. 1 cannot be uniquely described in the mixture-fraction domain. For example, several locations on the flame along the centerline have the same mixture-fraction value of 0.63 (Fig. 2), while the temperatures at these locations vary between 1195 and 1510 K.

The nonmonotonic variation in mixture fraction across the flame, shown in Fig. 2, is specific to the hydrogen/air opposing-jet flow considered in this study.

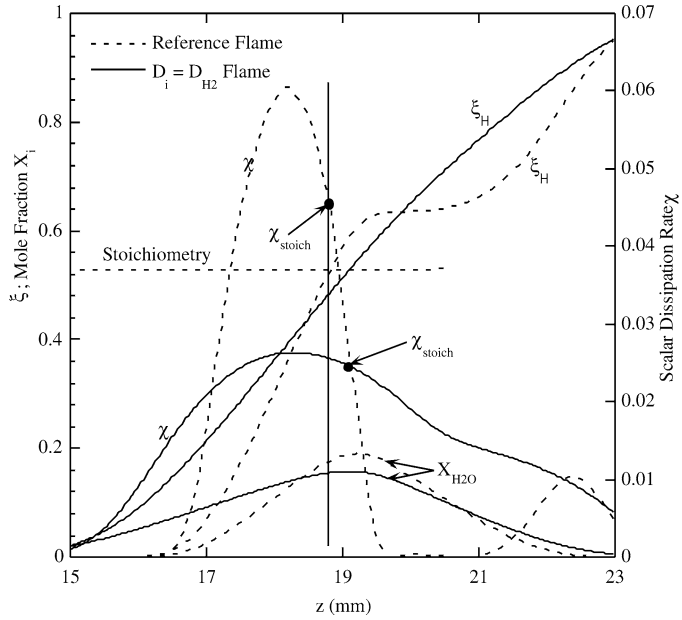

Fig. 3. Mixture fraction and scalar dissipation rate along the centerline for the reference flame (broken lines) and "$D_i = D_{H_2}$" flame (solid lines).

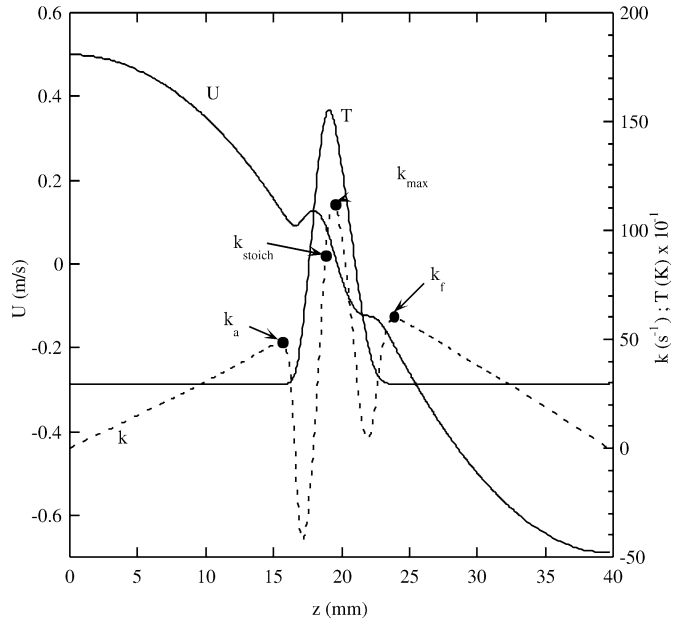

Fig. 4. Velocity, temperature, and strain rate along the centerline for the steady-state flame shown in Fig. 1.

To investigate whether such behavior appears in other forms of mixture fractions, variations of mixture fractions obtained from the elemental mass fractions of the oxygen atom (ξ_O) [37] and the hydrogen and oxygen atoms ($\xi_{H\&O}$) [39] are displayed in Fig. 2 using solid and open symbols, respectively. Note that the latter form of mixture fraction was proposed by Bilger [39] to take into account the preferential-diffusion effects associated with hydrogen flames. The stoichiometric mixture fraction for all three forms is 0.5264. The mixture fraction (ξ_O) obtained using the element originating from the oxidizer jet (which is O) increases smoothly with distance, and stoichiometry occurs at $z = 19.66$ mm (Location C), which is on the fuel side of the reaction zone. As expected, the mixture fraction ($\xi_{H\&O}$) calculated based on elements

originating from both the fuel and the oxidizer jets falls between ξ_H and ξ_O, and stoichiometry occurs at $z = 19.45$ mm (Location D).

Since the mixture fraction is extensively used in characterizing the structure of a diffusion flame, it is useful to identify the underlying flame properties for the nonmonotonic behavior of the mixture fraction. In laminar nonpremixed flames, mixing takes place through diffusion only; and if the diffusivities of all species are equal, then the mixture fraction becomes an independent variable with respect to the choice of species. However, in hydrogen flames the diffusivity of hydrogen (into nitrogen) is approximately three times that of oxygen, and the mixture fraction does not become an independent variable ($\xi_H \neq \xi_O \neq \xi_{H\&O}$), as shown in Fig. 2. To demonstrate the preferential-diffusion effect on mixture fraction, calculation of the steady flame in Fig. 1 is repeated by assuming that the diffusion coefficients of all of the species are identical to that of hydrogen and by enforcing the Le = 1 condition for heat transport. The distributions of fuel and oxygen concentrations and the mixture fraction for the "$D_i = D_{H_2}$" flame are shown in Fig. 2 with solid lines. The flame became thicker than the reference flame as a result of increased oxygen diffusion. In this "$D_i = D_{H_2}$" flame, the mixture fraction was monotonically increased to unity from zero, and the stoichiometric value (0.5264) appeared at $z = 19.1$ mm (Location B), where the mole fraction of oxygen is nearly twice that of hydrogen.

In the reference flame oxygen diffuses much more slowly (∼0.3 times) than hydrogen. Because of this lower diffusivity, the oxygen-concentration profile on the air side is steeper (Fig. 2) than that in the "$D_i = D_{H_2}$" flame; this, in turn, causes the mixture-fraction (ξ_H) profile to be steeper on the air side. Similarly, water diffuses more slowly in the reference flame than in the "$D_i = D_{H_2}$" flame. This increases the water concentration in the flame zone (Fig. 3) and, thereby, the local value of the mixture fraction—leading to a peak in the profile. Note that the stoichiometric value of the mixture fraction in the reference flame appears at a location that is slightly shifted from the stoichiometric condition based on the reactant mole fraction (i.e., $X_{O_2} = 2X_{H_2}$) toward the air side. In fact, none of the mixture-fraction definitions yielded stoichiometric conditions at their respective stoichiometric values.

The scalar dissipation rate χ is often used to characterize a stretched diffusion flame. Based on the mixture fraction, χ is defined as

$$\chi = 2D\left[\left(\frac{d\xi}{dz}\right)^2 + \left(\frac{d\xi}{dr}\right)^2\right]. \tag{2}$$

Here, D is the diffusion coefficient and, for simplicity, may be considered to be 1 m/s^2. Variations of the scalar dissipation rate and the mole fractions of H_2O along the centerline are shown in Fig. 3 for both the reference and the "$D_i = D_{H_2}$" flames. The steep gradient in ξ_H in the former flame resulted in values of χ that were significantly higher than those obtained in the latter flame. Furthermore, the reference flame exhibits more than one peak in the χ distribution; this is true for all of the scalar-dissipation-rate profiles that were obtained for this flame by employing various mixture-fraction definitions. The existence of double peaks in the scalar dissipation rate is a particular characteristic of a diffusion flame in which preferential-diffusion and non-unity-Lewis-number effects are significant. The stoichiometric values of the scalar dissipation rates for both reference and "$D_i = D_{H_2}$" flames are indicated in Fig. 3 by solid circles. In both flames the maximum scalar dissipation rates occur on the air side of the stoichiometric location. The peak value of χ in the reference flame is about 20% higher than that at stoichiometric location and appears ∼1 mm on the air side. Since there is no particular advantage in using one form of scalar dissipation rate over the other for characterizing a hydrogen diffusion flame, the scalar dissipation rate calculated from Eq. (1) is used in the present study for convenience.

The velocity, temperature, and strain-rate distributions along the centerline for the steady flame are shown in Fig. 4. Several investigators have used strain rate to characterize an opposing-flow jet diffusion flame. However, as seen in Fig. 4, this flame has no single (or unique) strain rate. The various strain rates that can be defined for this flame are as follows:

(1) global strain rate based on nozzle separation and exit velocities (k_{glob}) = 29.75 s^{-1},
(2) air-side strain rate (k_a) = 48.9 s^{-1},
(3) fuel-side strain rate (k_f) = 59.6 s^{-1},
(4) strain rate at the stoichiometric surface (k_{stoich}) = 68.9 s^{-1},
(5) peak strain rate (k_{max}) = 112.5 s^{-1}.

The air- and fuel-side strain rates are obtained from the locations where the temperature initially begins to increase from room conditions on the respective sides. In a steady-state flame, as shown in Fig. 4, the air- and fuel-side strain rates match the local peak values on the respective sides of the flame zone. However, such a criterion does not necessarily hold in the case of unsteady flames. Therefore, k_a and k_f are obtained from the temperature gradient rather than the peak values for all of the unsteady flames discussed in the present paper.

The steady-state flame shown in Fig. 2 represents a weakly strained laminar flame. The peak strain rate

on the fuel side is greater than that on the air side as a result of the difference in the density of the two jets. Even at this low strain rate, the fuel and oxidizer are not completely consumed simultaneously in the flame zone. In an overlap region of ~2 mm, both H_2 and O_2 are present (cf. Fig. 2). The flame (peak-temperature region) is located at $z = 19.2$ mm, and its temperature of 1560 K is only slightly lower than the corresponding adiabatic equilibrium temperature of 1598 K.

The steady-state strain rate of the opposing-jet flame can be increased by gradually increasing the velocities of the fuel and air jets. Calculations were repeated with the jet velocities being varied, and it was found that a stable steady-state flame could be obtained for fuel and air jet velocities of 16 and 14 m/s, respectively. These velocities yielded an air-side strain rate (k_a), a fuel-side strain rate (k_f), and a strain rate at the stoichiometric surface (k_{stoich}) of 1410, 1678, and 2460 s^{-1}, respectively. The maximum scalar dissipation rate ($\chi_{\max}$) and the scalar dissipation rate at the stoichiometric surface (χ_{stoich}) for this extinction condition are 1.28 and 0.78, respectively. The corresponding peak (flame) temperature was 1130 K. The extinction strain rate and flame temperature agree favorably with calculations made by Gutheil et al. [40]. A small increase in either air- or fuel-jet velocity from these extinction limits first caused the flame temperature to decrease below 1130 K and then caused the flame to extinguish, with its temperature reaching 300 K in <1 ms. Based on these calculations a steady-state-extinction criterion of 1130 K has been established and was used in the later studies on unsteady flame extinction. Analysis of unsteady flames (shown in a later section) suggested that the 1130-K criterion for defining extinction is valid for unsteady flames also.

An unsteady strain rate was imposed on the flame shown in Fig. 1 by issuing vortices simultaneously from the fuel (top) and air (bottom) nozzles. Various unsteady flames were generated by injecting air and fuel through the respective syringe tubes in such a way that the peak values of the exit velocities were in the range of 2–19 m/s. In the following sections, the dynamics associated with these vortices is discussed, followed by the changes to the flame structure caused by the impingement.

3.3. Interaction with colliding vortices of different sizes

Vortices are shot toward the flame surface simultaneously from the air and fuel sides by injecting a specified amount (2.2 cm^3) of air and fuel through the respective syringe tubes. The flame-quenching process with colliding vortices of different sizes is studied by injecting air through a 5-mm-diameter injection tube and fuel through a 2-mm-diameter injection tube. Evolution of the vortices and their interaction with the flame surface depend on the injection duration. In general, with shorter injection durations, the generated vortices travel faster toward the flame surface and affect its structure as the local-flow time scales approach the chemical time scales. Calculations and measurements are performed to capture the colliding-vortex/flame-interaction process for various injection velocities.

While calculations for peak injection velocities of <2 m/s yielded flames that were stretched and wrinkled but not extinguished anywhere, calculations for higher velocities resulted in flame quenching along the stagnation line and propagation of the flame edge into the multivortex flowfield. Experiments were also performed for some of the injection conditions in an attempt to understand the flame-quenching pattern during the vortex–flame–vortex interaction process. The computed and experimental results for the +5/−5-m/s injection case at different stages of the interaction process are shown in Fig. 5. The computed temperature and OH-concentration distributions are plotted on the left and right halves of Figs. 5a–5c. The instantaneous locations of the particles that were released from the air and fuel nozzles are also shown in these figures to aid visualization of the flow structures. Air injected from the 5-mm-diameter tube generated a vortex, and it grew to 12 mm in diameter by the time (8.1 ms) it reached the flame surface (Fig. 5a). Similarly, during the same time period, the fuel vortex grew to 5 mm from its initial size of 2 mm. The collision of these two vortices at the flame surface stretched the flame. The temperature of the flame along the stagnation line decreased to 1140 K, which is near the quenching limit of 1130 K. In another millisecond, the double-vortex/flame interaction completely quenched the flame that was sandwiched between the vortices in the region around the centerline (Fig. 5b). As the vortices continued to push against each other in the hole formed on the flame surface, the edge of the flame wrinkled and propagated into the fuel vortex, as evident in Fig. 5c. Similar behavior was observed in the OH-concentration distributions obtained in the experiment through the use of the planar laser-induced-fluorescence (PLIF) technique (Figs. 5d–5f). Details of the PLIF measurements made in the Rolon burner are given in Refs. [41,42]. Considering the difficulties associated with the alignment of the small tubes that were separated by 40 mm, the symmetric nature of the flowfield obtained in the experiments during the double-vortex/flame interactions is reasonable. The predictions are qualitatively in good agreement with the measurement results. The injection velocities for the vortices in the present calculations were estimated

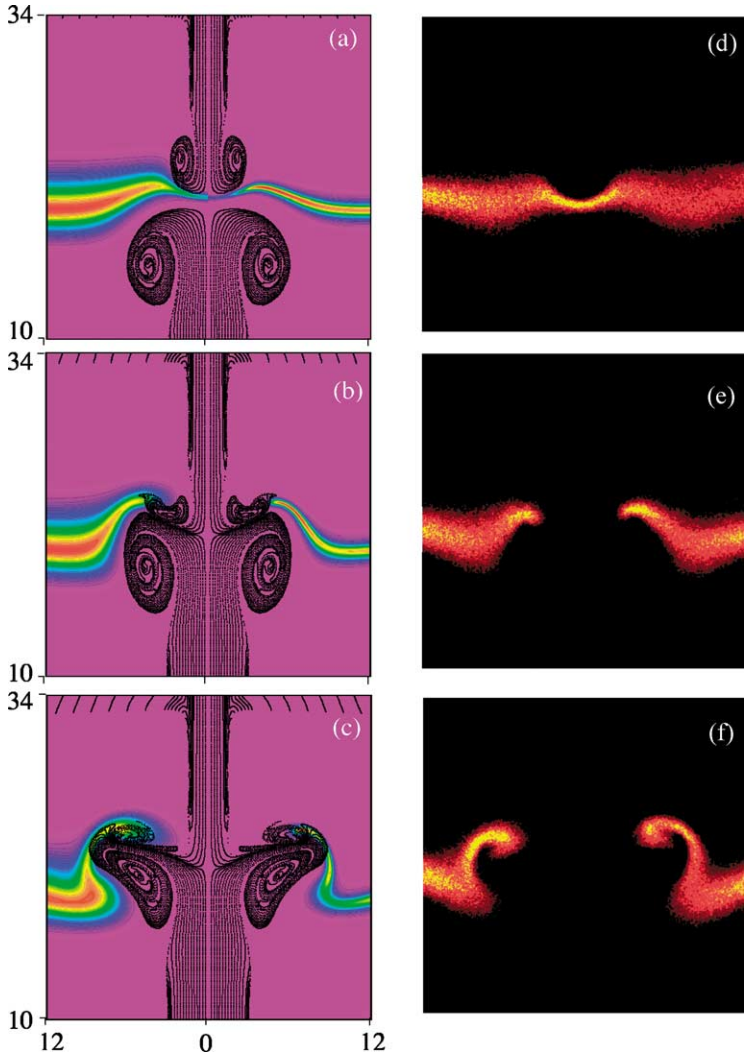

Fig. 5. Comparison of simulated ((a), (b), and (c)) and measured ((d), (e), and (f)) double-vortex/flame interactions at various instants. Particle locations are superimposed on temperature (left) and OH (right) fields of computed data. Raw data from PLIF of OH shown in experimental images. (a) and (d) at t_0 ms, (b) and (e) at $t_0 + 1$ ms, and (c) and (f) $t_0 + 2$ ms.

from the total amounts of fluid used for injections in the experiment—not from the actual velocities—which may have contributed to the discrepancy noted between the experiments and calculations in Fig. 5.

The collision of vortices of different sizes at the flame surface not only generated unsteady stretching on the flame but also shifted the flame location during the interaction process. As discussed earlier and in Ref. [23], the translation velocity of the flame during a vortex/flame-interaction process alters the extinction strain rate, thereby complicating the relationship between the unsteady strain rate and extinction. To alleviate this problem, investigations were performed by injecting vortices of the same size from the fuel and air sides simultaneously. This was achieved through the utilization of 5-mm-diameter injection tubes on both the air and the fuel sides.

3.4. Interaction with colliding vortices of the same size

A wide range of strain rates was imposed on the flame by forcing vortices from the fuel- and air-injection tubes simultaneously by (1) changing the maximum injection velocity and (2) changing the rise times, as shown in Fig. 6. Here, the imposed velocity with respect to time at the exit of the air-injection tube is shown for different injection schemes. Identical negative-velocity profiles were superimposed on the steady flow emanating from the fuel-injection tube.

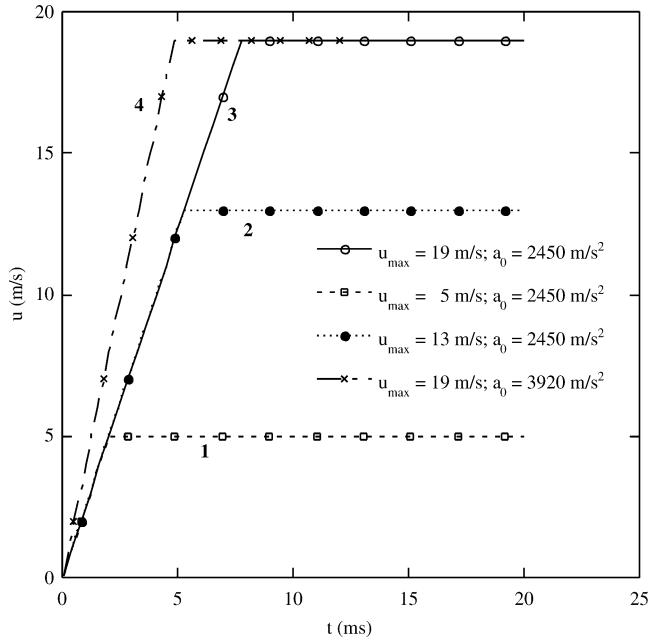

Fig. 6. Imposed velocity profiles at exits of fuel and air nozzles for generating various types of double-vortex/flame interactions.

In the case where the maximum velocity ($u_{\max}$) was changed, the rate of increase (a_0) for the imposed velocity was set at 2450 m/s^2 (for example, 1, 2, and 3 in Fig. 6); and in the case where the rise times were changed, the maximum velocity was set at 19 m/s (for example, 3 and 4 in Fig. 6). Calculations were performed for each case until the interaction reduced the flame temperature to 1000 K, which was well below the extinction temperature of 1130 K.

Vortex and flame structures at two instants for two cases with different maximum velocities are shown in Fig. 7. In both cases, the rate of increase for the superimposed velocity was set at 2450 m/s^2, and the maximum velocities were set equal to 5 m/s for the first case (Figs. 7a and 7b) and 13 m/s for the second case (Figs. 7c and 7d). Temperature is shown on the left side, and OH-concentration distributions are shown on the right. Instantaneous locations of the particles are superimposed on the temperature-OH plots to display the structures of the fuel and air vortices. The imposed velocity functions that generate these vortices are shown as Profiles 1 and 2 in Fig. 6. The injection velocity with a 5-m/s maximum value, failed to cause flame extinction. The temperature decreased to 1190 K in 8.35 ms (Fig. 7b) and then remained at this value during the remainder of the interaction process. It is evident from Fig. 7 that the flame did not travel axially while being stretched between the fuel- and air-side vortices for both velocity cases. In fact, for all of the velocity cases considered for colliding vortices of the same size, the flame did not travel while being dynamically stretched; this established a stationary unsteady (no translational component) strain rate on the flame. The flame in the 13-m/s-maximum-velocity case was nearly extinguished at the centerline in 6.1 ms (Fig. 7d), and the temperature decreased to 1190 K.

3.5. Unsteady flame structure

The flame structures along the centerline at three instants for the +13/−13-m/s interaction case are shown in Fig. 8. As the flame was being stretched, its thickness and temperature decreased, while the peak-temperature location remained nearly the same ($z \sim 19.2$ mm). Also, the reactant fluxes (gradients) near the flame zone increased with flame stretch. The amounts of fuel and oxygen crossing the flame (Fig. 8) due to nonequilibrium chemistry increased with flame stretch. The variations in strain rate, mixture fraction, and scalar dissipation rate along the centerline at 5.7 and 6.1 ms are shown in Figs. 9 and 10, respectively. The important quantities k_a, k_f, k_{stoich}, χ_{stoich}, and $\chi_{\max}$ are represented in these figures by filled circles. While the strain-rate distributions in the flame that is sandwiched between the two vortices are quite different from that of the steady-state flame, the scalar-dissipation-rate distributions in unsteady and steady-state flames remain similar. Even though the strain rate has increased significantly ($\sim$2000 s^{-1}) on both sides of the flame at 5.7 ms (Fig. 9), this high strain rate has not yet applied on the flame surface. Air- and fuel-side strain rates have increased only to

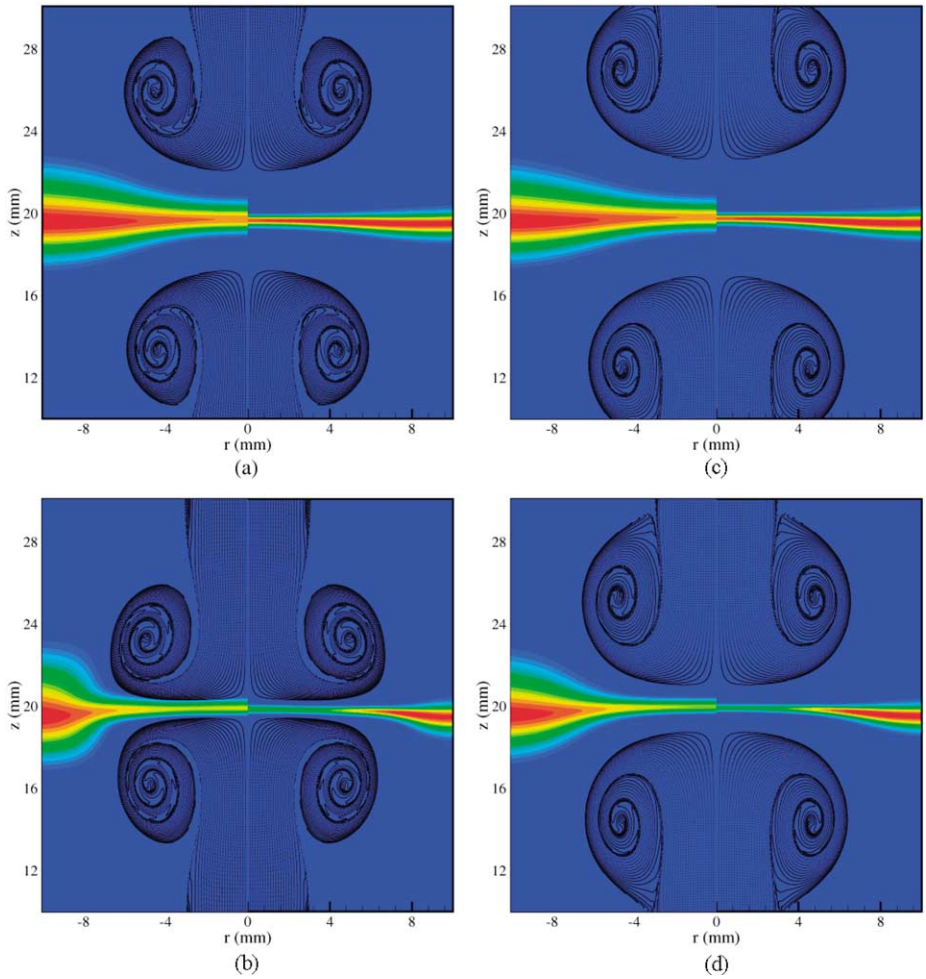

Fig. 7. Interaction of equal-sized counter-traveling vortices with flame at different instants: (a) and (b) for 5-m/s and (c) and (d) for 13-m/s peak-injection-velocity cases. Isotemperature and OH-mole-fraction contours are plotted on the left and right sides, respectively.

1120 and 1416 s^{-1}, respectively, while the maximum scalar-dissipation rate has increased to 1.03 s^{-1}.

At $t = 6.1$ ms the flame temperature decreased to 1150 K, and quenching of the flame was not observed. However, the air- and fuel-side strain rates increased to values that were well above the corresponding steady-state strain rates for extinction. Interestingly, the stoichiometric value of the scalar-dissipation rate deviated significantly from its maximum value (Fig. 10).

3.6. Extinction criterion for unsteady flames

The unsteady hydrogen flame is considered to be extinguished when its temperature falls below 1130 K, based on the steady-state-extinction criterion discussed earlier. Defining an extinction criterion for unsteady flames based on a critical temperature seems appropriate since the chemical kinetics and the heat-release rate (or temperature) are closely associated and such a criterion is often used in determining the extinction concentrations for fire-extinguishing agents [43,44]. The accuracy of this approach is evaluated in this section by investigating several unsteady flames under near-extinction conditions. Variations of flame temperature and heat-release rate with time during a slow, a moderate, and a fast vortex/flame interaction are shown in Fig. 11a. Similarly, the variations in peak production and destruction rates of the OH radical are shown in Fig. 11b, and those of the H radical are shown in Fig. 11c.

As the stretch on the flame is increased, increasingly more reactants are forced into the flame zone. As a result, (1) consumption of reactants in the flame zone increases—yielding an increase in the heat-release rate—and (2) the temperature decreases as

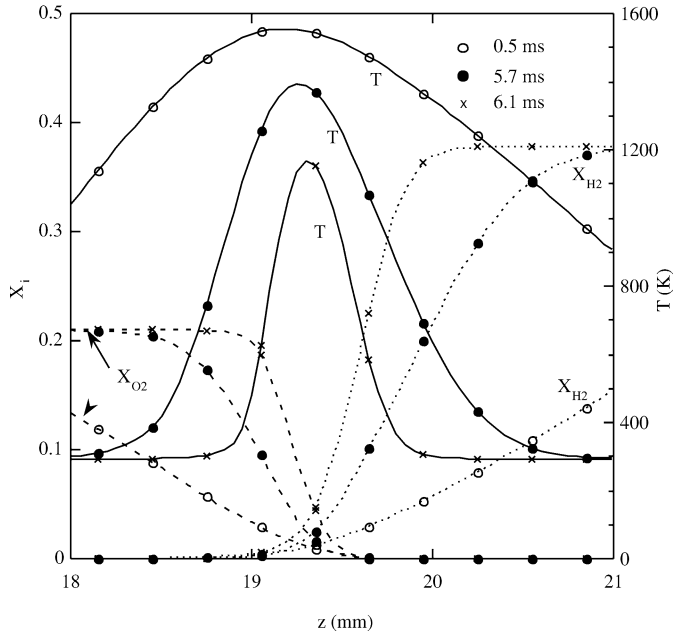

Fig. 8. Instantaneous structures of flame during double-vortex/flame interaction produced using 13-m/s injection velocity.

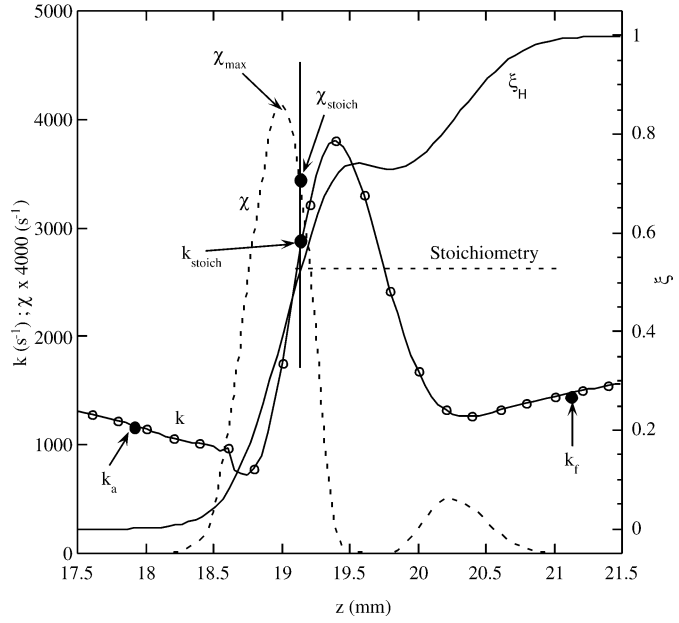

Fig. 9. Mixture fraction, scalar dissipation rate, and strain rate along the centerline at $t = 6$ ms during double-vortex/flame interaction produced using a 13-m/s injection velocity.

a result of the inability of the flame to consume (burn) all of the reactants. An increase in reactant consumption also increases the production and destruction rates for all of the species, with the exception of the OH radical. The production rate of OH decreases monotonically, as shown in Fig. 11b, to zero as the flame is stretched. In any case, once the flame begins to extinguish, all the quantities in Fig. 11 decrease rapidly. It is important to note that extinction of a flame is not an instantaneous event but a process which takes place over a period of time. In flame studies, however, the instant at which the extinction process begins is of most interest and is the one investigated in the present study. In steady-state

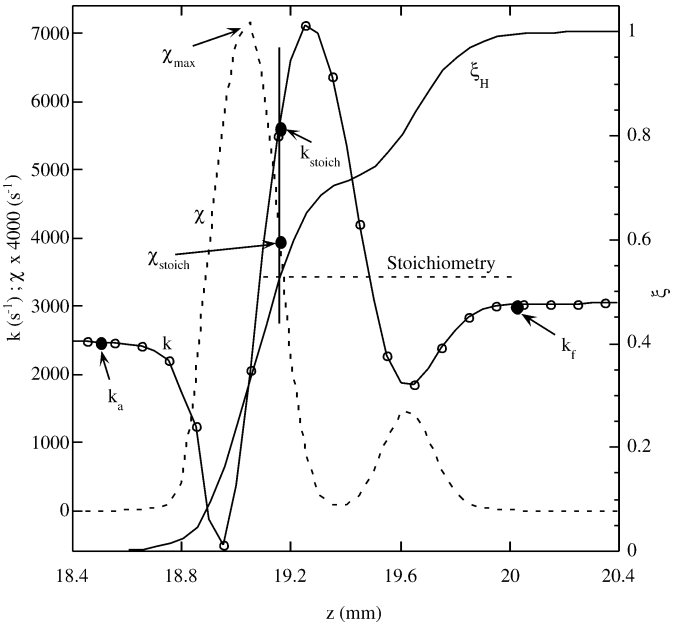

Fig. 10. Mixture fraction, scalar dissipation rate, and strain rate along the centerline at $t = 7$ ms during double-vortex/flame interaction produced using 13-m/s injection velocity.

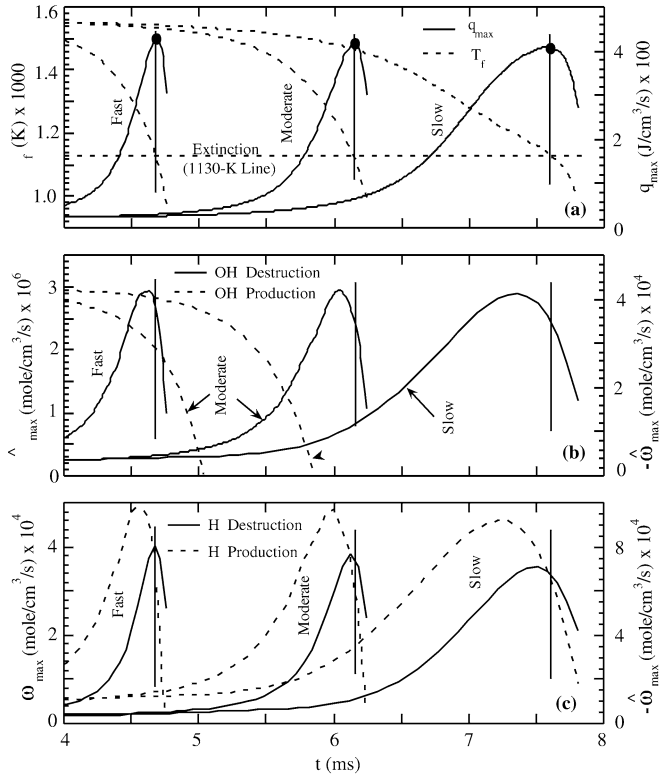

Fig. 11. Changes in characteristic flame quantities in the neighborhood of extinction when the flame is subjected to slow-, moderate-, and fast-changing strain rates. (a) Temperature and heat release rate, (b) OH production and destruction rates, (c) H production and destruction rates.

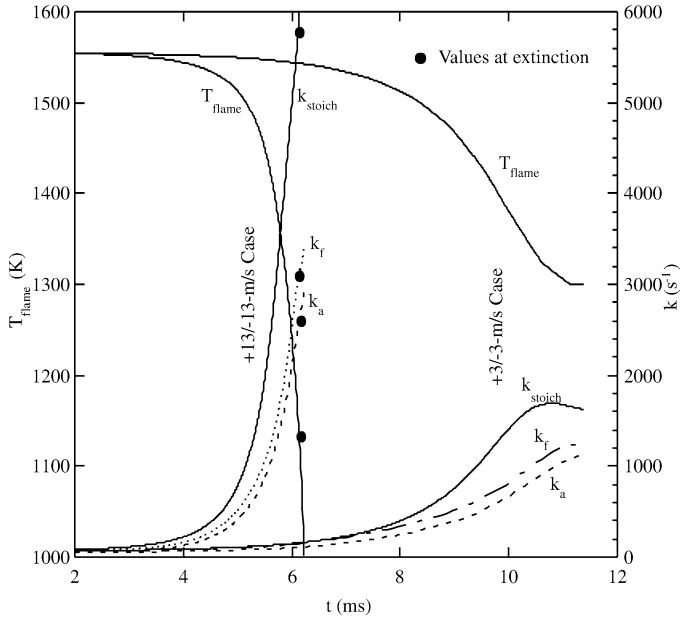

Fig. 12. Variations of flame temperature and strain rates with time during two double-vortex/flame interactions.

flames it was observed that the temperature and heat-release rate increase with stretch rate and that the extinction process begins when the flame temperature decreases to 1130 K. As evident from Fig. 11a, the heat-release rate in unsteady flames also reaches a maximum value when the temperature decreases to 1130 K, and any further decrease in temperature is associated with a sharp decrease in heat-release rate. This temperature/heat-release-rate behavior is the same in all of the unsteady flames simulated using a wide range of vortex velocities (or vortex/flame-interaction times) and strongly correlates with the behavior observed in steady-state flames. Consequently, the 1130-K criterion found in steady-state flames is extended to unsteady flames for determining the time at which extinction begins. Interestingly, OH and H destruction rates (Figs. 11b and 11c) reach their peak values slightly before the temperature decreases to 1130 K, and production of OH ceases ∼1 ms prior to this event. For the fast vortex/flame interaction, OH production ceased at $t = 3.6$ ms and was not apparent in Fig. 11b.

3.7. Characterization of extinction in unsteady flames

Simulations made for various double-vortex/flame interactions resulted in local flame extinction along the centerline. Traditionally, extinction is characterized by the strain rate imposed on the flames [1,3]. However, it has been shown by several authors that the strain rates at which unsteady flames are extinguished are significantly higher than those at which steady-state flames are extinguished [9,23]. Since the strain rate has been found to be an inadequate quantity for describing the extinction behavior of an unsteady flame, several researchers have examined other variables that might be used for this purpose. The variable often used is the scalar dissipation rate [45]. The results obtained for double-vortex/flame interactions in the present study were used to investigate the adequacy of the strain rate and scalar-dissipation rate for describing the quenching process associated with unsteady flames.

3.8. Vortices with different injection masses

The double-vortex/flame interaction shown in Figs. 7a and 7b stretched the flame significantly but did not cause flame extinction. On the other hand, the interaction shown in Figs. 7c and 7d caused local extinction. These two interactions were obtained by injecting fluids at different peak velocities. The changes in temperature and various strain rates during these interaction processes are shown in Fig. 12. When the injection peak velocity was 3 m/s, the flame temperature gradually decreased to ∼1300 K and then remained at that level, accompanied by some weak oscillations (∼20 K in magnitude). Typically, soon after the collision at the flame surface, the double vortices generate secondary vortices; this, in turn, creates oscillations in the flame temperature. Nevertheless, for this injection the flame was not extinguished. The air-side strain rate increased, as expected, with time dur-

ing the double-vortex/flame interaction and reached a maximum value of 1080 s^{-1}. This value is well below the steady-state extinction strain rate of 1410 s^{-1}; hence, flame quenching would not be expected for this injection condition. The fuel-side strain rate and that at the stoichiometric location also increased with time during the interaction process. Interestingly, the stoichiometric strain rate began to deviate increasingly from k_a and k_f as the flame was stretched.

Similar plots for the 13-m/s peak-injection-velocity case are also shown in Fig. 12. In this case the flame temperature decreased rapidly to room temperature, with flame quenching occurring at ~1130 K. As discussed earlier, this temperature limit was obtained from the steady-state quenching study. The temperature and various strain rates at the instant of flame extinction are indicated by solid circles in Fig. 12 for the 13-m/s peak-injection case. It should be noted that the air-side strain rate at the time of extinction is ~2600 s^{-1}, which is nearly twice that required to quench the flame in a steady-state manner. The air- and fuel-side strain rates seem to increase at the same rate during the interaction process; the stoichiometric strain rate, on the other hand, increases much more rapidly, and the value at extinction (~5750 s^{-1}) is nearly 2.3 times that obtained for a steady-state flame.

To aid the understanding of the extinction behavior of an unsteady flame, the temperature and strain-rate behavior for all of the peak-injection-velocity cases are plotted in Figs. 13 and 14, respectively. Flame extinction is observed only for the cases with peak injection velocities greater than 5 m/s. As the peak injection velocity is increased above this value, the flame temperature decreases rapidly. However, the response of the flame to the changes in peak injection velocity diminishes at higher peak values. For example, the decrease in temperature remains nearly the same for the 12- and 13-m/s peak-injection cases. Note that all of the double-vortex/flame interactions shown in Figs. 13 and 14 were obtained by imposing the same rate of increase for different peak-injection-velocity cases, as shown in Fig. 6. This suggests that in the higher peak-injection-velocity cases, the primary vortex growth—and, thereby, flame extinction—occurs prior to the injection velocity actually reaching the peak value, which renders a further increase in the maximum velocity trivial with regard to the flame-extinction process.

The increases in air-side strain rate (k_a) during various double-vortex/flame interactions are shown in Fig. 14. The extinction conditions for cases with peak injection velocity >5 m/s, determined based on the 1130-K temperature limit, are indicated by filled-circles. The envelope passing through these circles separates the flame from its extinction state. In general, the strain rate at which extinction takes place increases with applied maximum injection velocity. It is also evident from this figure that an opposing-jet flame survives at a strain rate that is much higher than the steady-state extinction limit (1410 s^{-1})—if the flame is subjected to that strain rate rapidly. In other words, the faster the flame stretches, the higher the strain rate it can withstand without being quenched. Similar behavior was observed in other characteristic parameters such as k_f, k_{stoich}, $\chi_{\max}$, and χ_{stoich}.

Vortices generated using a fixed rate of increase ($a_0 = 2450$ m/s^2) in injection velocity traveled toward the flame surface and caused the flame to stretch. However, as evident in Figs. 13 and 14, the stretch applied on the flame surface did not increase in proportion to the peak value of the injection velocity, and the maximum imposed air-side strain rate was limited to ~2635 s^{-1} because of the apparent saturation in vortex-penetration velocity. Vortices generated with peak values >10 m/s caused extinction prior to the injection velocity reaching its specified peak value; thus, the peak value became trivial with regard to the quenching process. To circumvent this saturation problem, vortices were generated by injecting fluid at different rates of increase in the injection velocity (2450–4900 m/s^2) and by maintaining the peak injection velocity at 19 m/s, as shown in Fig. 6. Such a high peak value was chosen to ensure that extinction would occur prior to the injection velocity reaching the peak value even at the slowest rate of injection (2450 m/s^2).

3.9. Vortices with the same injection mass

Calculations for the double-vortex/flame interactions were made using the above-mentioned constant-peak-velocity injection scheme. The changes in flame temperature along the centerline during the interaction process for all of the cases are plotted in Fig. 15. The extinction process in the flame was considered to begin when the temperature decreased to 1130 K. Further decrease in temperature after the flame is locally extinguished results from the diffusion and conduction of products and heat, respectively, from the flame zone. As expected, the flame responds uniquely to changes in the acceleration of fluid injection. The time at which extinction occurs is inversely proportional to the rate of increase (a_0) in the injection velocity.

The changes in air-side strain rate during the vortex/flame-interaction process are shown in Fig. 16 for various a_0 cases. The stain rates at which extinction took place were obtained from the 1130-K-cutoff criterion and are indicated by filled circles in this figure. A linear decrease in extinction strain rate with time can be observed. All of the interactions in Fig. 16 occur more rapidly than those in Fig. 14 and are

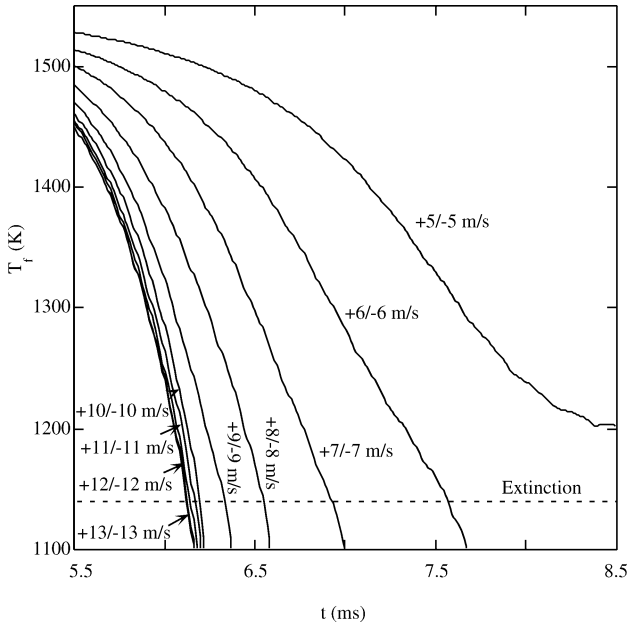

Fig. 13. Variations of flame temperature with time for double-vortex/flame interactions simulated using various peak injection velocities.

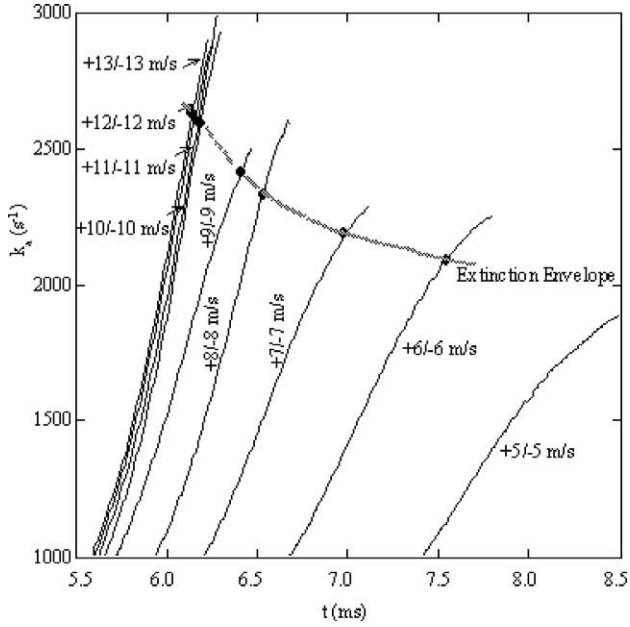

Fig. 14. Variations of air-side strain rate with time for double-vortex/flame interactions simulated using various peak injection velocities.

sustained to much higher air-side strain rates. The extinction strain rate increased from 2600 to 3200 s^{-1} when the injection-fluid accelerations were increased from 2450 to 4900 m/s^2. The data in Figs. 14 and 16 clearly indicate that using a unique value of air-side strain rate, one cannot predict the quenching condition of an unsteady flame. In other words, the value of the air-side strain rate at which extinction occurs in an unsteady flame depends on the rate at which the flame was strained. Changes in fuel-side and stoichiometric strain rates with time for various double-vortex/flame interactions (for $u_{max} = 19$ m/s cases) are plotted

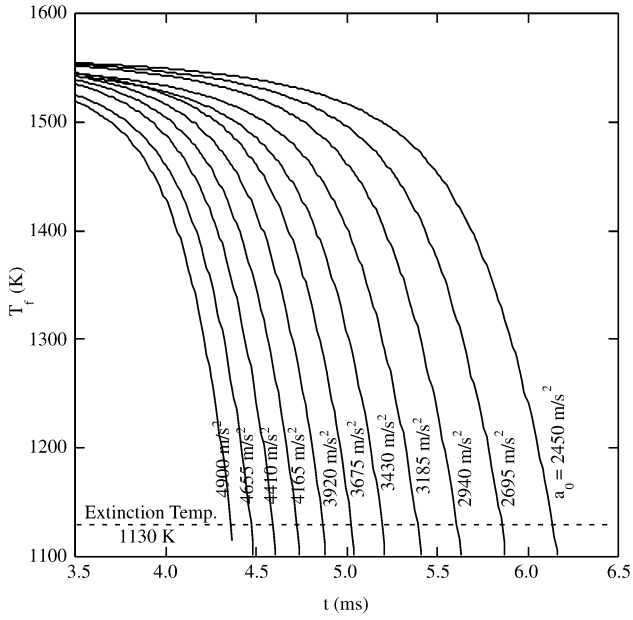

Fig. 15. Variations of flame temperature with time for double-vortex/flame interactions simulated using various rates of increase in injection velocity.

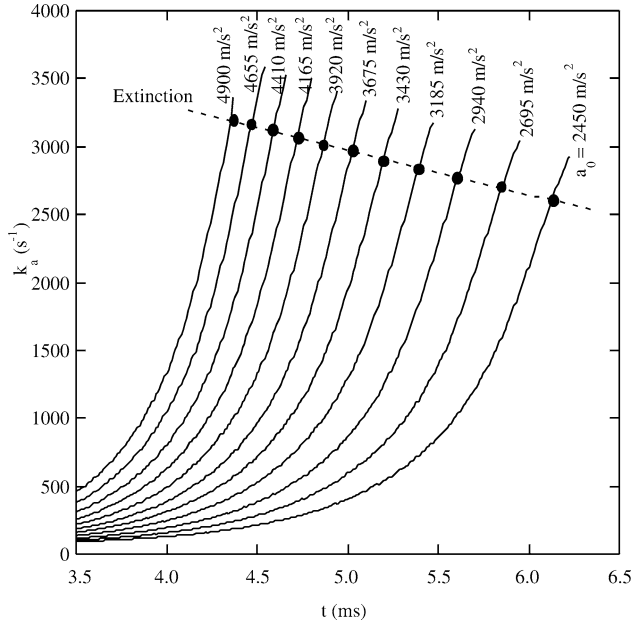

Fig. 16. Variations of air-side strain rate with time for double-vortex/flame interactions simulated using various rates of increase in injection velocity. Extinction values based on the 1130-K-temperature criterion are indicated by solid circles.

in Figs. 17 and 18, respectively. Similar to the behavior of the air-side strain rate, both the fuel-side and the stoichiometric strain rates increase with time. It is important to note that these extinction-strain-rate values (obtained from the 1130-K-cutoff criterion and indicated by solid circles) also decrease with time—similar to the behavior of the air-side strain-rate values. Figs. 15–17 suggest that none of these strain rates can characterize an unsteady extinction process uniquely. However, among the three strain rates, the air-side one is the least sensitive to unsteadiness. It decreased by only 585 s^{-1} when the vortex interaction time was increased by 1.77 ms, while the fuel-side and stoichiometric strain rates decreased by

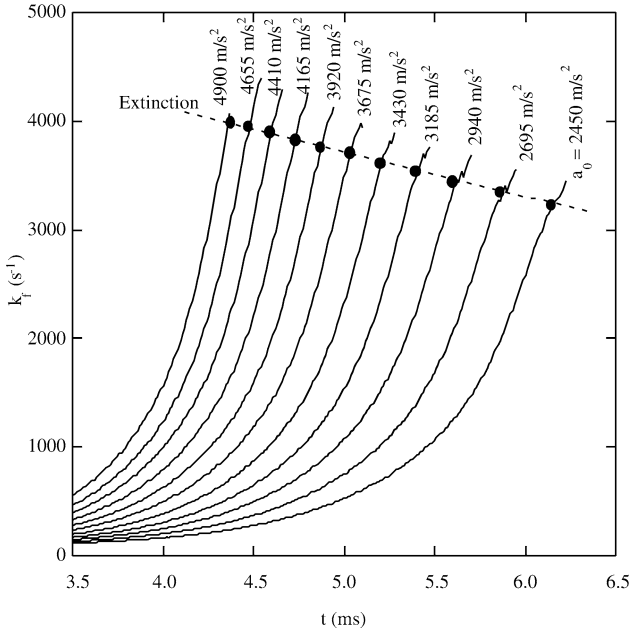

Fig. 17. Variations of fuel-side strain rate with time for double-vortex/flame interactions simulated using various rates of increase in injection velocity. Extinction values based on the 1130-K-temperature criterion are indicated by solid circles.

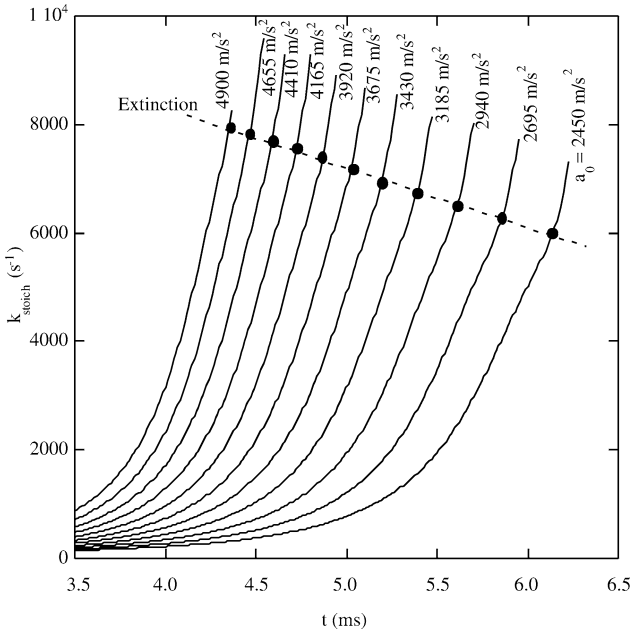

Fig. 18. Variations in strain rate at the stoichiometric location with time for double-vortex/flame interactions simulated using various rates of increase in injection velocity. Extinction values based on the 1130-K-temperature criterion are indicated by solid circles.

860 and 2000 s^{-1}, respectively. The reason for the dependence of extinction strain rate on vortex–flame interaction time is explained below.

The structures along the centerline of a slowly strained flame ($a_0 = 2450$ m/s^2) and a rapidly strained flame ($a_0 = 4099$ m/s^2) just prior to extinction are compared in Fig. 19. The fuel and oxygen fluxes (gradients) into the flame zone, the temperature distributions, and the widths are nearly identical for both flames (Fig. 19a). The mixture-fraction (ξ_H) dis-

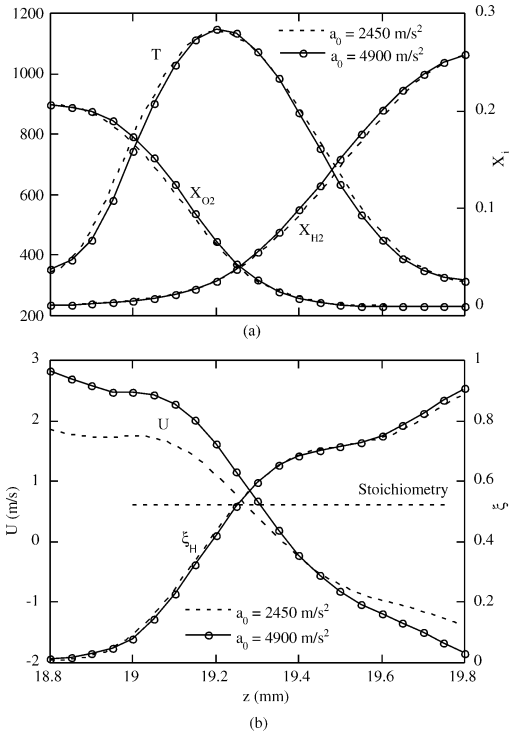

Fig. 19. Comparison of structures along the centerlines of slowly and rapidly strained flames at time of extinction. (a) Temperature and reactant mole fractions; (b) velocity and mixture fraction.

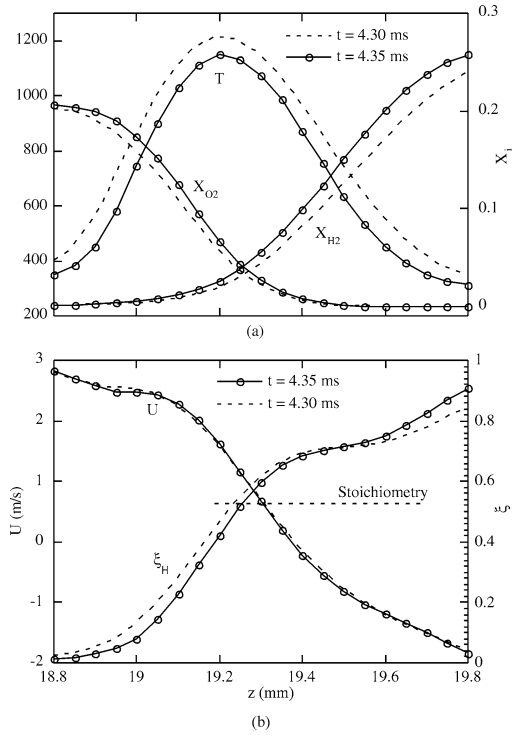

Fig. 20. Comparison of structures along the centerline at two instants near extinction for a rapidly strained flame. (a) Temperature and reactant mole fractions; (b) velocity and mixture fraction.

tributions are also quite similar, as shown in Fig. 19b. For all practical purposes, based on the temperature and species distributions, one might consider these two flames to be chemically identical. However, as shown in Fig. 19b, their flow structures are quite different. The rapidly strained flame is subjected to higher velocity gradients (solid line) across the reaction zone than the slowly strained flame (broken line). Since strain rate describes the flow structure, the air-side, fuel-side, and stoichiometric strain rates are all higher for the former flame. That means that even though the chemical structures of the two flames are identical, the strain rates acting on them can be different if the flow structures are different.

In a diffusion flame, fuel and oxygen consumed in the reaction zone enter through convection and diffusion. On the other hand, convective flow also influences the fuel (or oxygen) distribution and, thereby, modifies the diffusion flux. For example, an increase in convective flow in the z direction in Fig. 19a brings more fresh oxygen into the flame zone; this, in turn, increases the oxygen-concentration gradient, eventually increasing the diffusive flux of oxygen into the flame zone. When a vortex travels toward the flame surface, it induces convective flow upstream of the vortex through a pressure wave. Consequently, through diffusion, the fluid in the vortex will be distributed in the region surrounding the vortex. However, since diffusion velocities are only on the order of 0.4 m/s (in a 0.8-mm-thick flame), a considerable delay will occur between the fluid diffusion and the velocity imposition—leading to a flow-nonequilibrium situation. The delay between the imposed velocity and the resulting diffusion was also observed by Egolfopoulos and Campbell [7] and Takahashi and Katta [46] in moderately strained flames.

The two flames shown in Fig. 19 are in a flow-nonequilibrium state, with diffusion not yet fully adjusted to the imposed velocity. As the delay between the diffusion and the imposed velocity increases with vortex-convection speed, the rapidly strained flame requires a longer period of time to achieve equilibrium than the slowly strained flame; the result is identical chemical but different flow structures.

To further verify the hypothesis concerning the flow-nonequilibrium situation in unsteady flames, the structures along the centerline for the rapidly strained flame ($a_0 = 4900$ m/s^2) at two instants are shown in Fig. 20. While the data represented by solid lines at $t = 4.35$ ms are those shown in Fig. 19 for this flame, those represented by broken lines were ob-

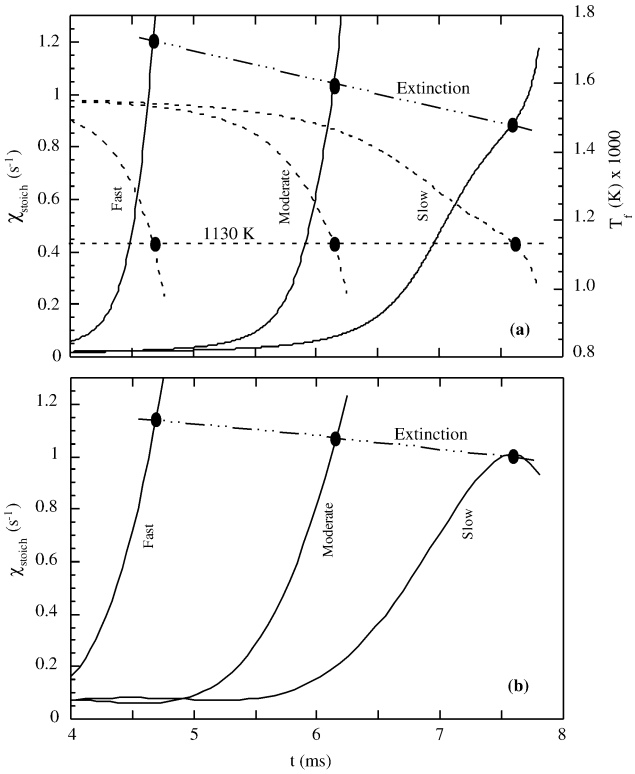

Fig. 21. Changes in scalar dissipation rates at stoichiometry in the neighborhood of extinction when flame is subjected to slow-, moderate-, and fast-changing strain rates. Scalar dissipation rates are calculated using mixture fractions defined based on (a) Bilger's formula [39] and (b) Eq. (1).

tained 0.05 ms earlier in the double-vortex/flame-interaction process. Although the vortices on the fuel and air sides of the flame have moved very near each other by $t = 4.3$ ms, the velocity has not changed appreciably during the following 0.05 ms (Fig. 20b) of interaction. However, as observed in Fig. 20a, the diffusion layer moved ∼0.02 mm toward the peak-temperature location. This movement is consistent with that estimated based on a diffusion velocity of 0.4 m/s. The increased fuel and oxygen flux into the reaction zone cooled the flame (decrease in T) and reduced the reactant consumption (increased amounts of fuel and oxygen at the stoichiometric surface).

Since the strain rate computed at a flame location represents the flow structure at that location and because of the flow nonequilibrium discussed previously, an accurate description of the quenching process using strain rate alone is not possible, as demonstrated in Figs. 14, 16, 17, and 18. In contrast, however, since the scalar dissipation rate (defined in Eq. (2)) represents the overall diffusion process, this rate calculated at a flame location could be used to describe the quenching process.

As described previously, Eq. (2) yields different forms of the scalar dissipation rate, depending on the mixture-fraction definition used. The sensitivities of the three scalar dissipation rates (obtained based on ξ_H, ξ_O, and $\xi_{H\&O}$) to the stretching time period of an unsteady flame are compared by computing these rates for the three vortex/flame interactions (slow, moderate, and fast) described in Fig. 11. In general, all of the four scalar-dissipation-rate profiles along the stagnation line during these three vortex/flame interactions are similar to the ones shown in Figs. 9 and 10, with two peaks occurring in the flame zone—one near the stoichiometric location and the other on the fuel side of the flame zone. The variations of scalar dissipation rate at stoichiometry with time during the three vortex/flame interactions are shown in Fig. 21. Only scalar dissipation rates obtained with Bilger's mixture fraction ($\xi_{H\&O}$) and H-element-based mixture fraction (ξ_H) are shown here (Figs. 21a and 21b, respectively). It should be recalled from Fig. 2 that the stoichiometric location of the Bilger's mixture fraction is nearest to the peak-reactivity location ($2X_{H_2} = X_{O_2}$ location), while that of the H-element-based mixture fraction is farthest from it. Extinction values determined based on the 1130-K criterion are also shown in Fig. 21. It is evident from this figure that the extinction scalar dissipation rates ob-

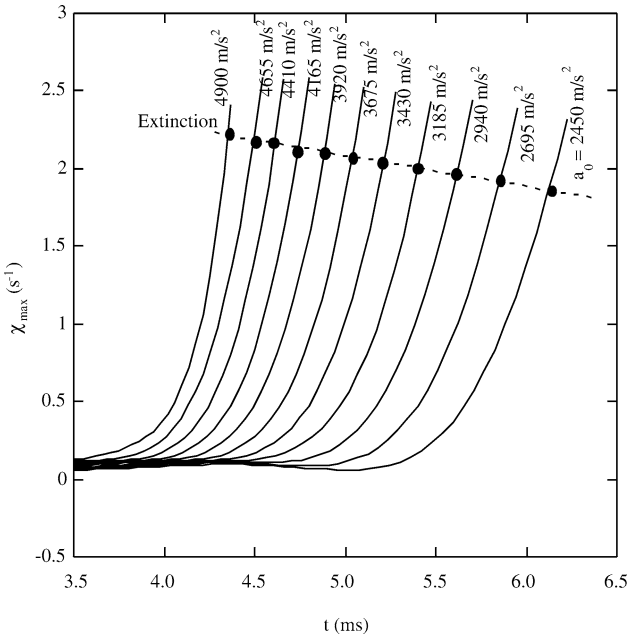

Fig. 22. Variations of the peak scalar dissipation rate with time for double-vortex/flame interactions simulated using different rates of increase in injection velocity. Extinction values based on the 1130-K-temperature criterion are indicated by solid circles.

tained with $\xi_{H\&O}$ (Fig. 21a) are more sensitive to the vortex/flame-interaction time than those obtained with ξ_H. In fact, based on sensitivity to interaction time (or vortex speed), the scalar dissipation rate obtained using ξ_H was least sensitive, followed by that obtained with $\xi_{H\&O}$, and, finally, that obtained with ξ_O. Because of the lowest sensitivity, the scalar dissipation rate obtained with ξ_H is used for the evaluation of the scalar dissipation rate for describing the extinction of unsteady flames.

Variations in the maximum value of the scalar dissipation rate and the local value at the stoichiometric surface with time are plotted for each double-vortex/flame-interaction case in Figs. 22 and 23, respectively. The respective values at extinction for all of the unsteady flames, determined based on the 1130-K criterion, are represented by filled circles. From Figs. 22 and 23, it is apparent that the scalar dissipation rates χ_{max} and χ_{stoich} also failed to characterize the extinction process in unsteady flames uniquely, which means that extinction in unsteady flames cannot be predicted using scalar dissipation rates. However, the variations in extinction values with respect to the changes in fluid-injection velocity seem to be smaller for scalar dissipation rates than for strain rates. The ranges in unsteady extinction values of various characteristic variables used in the present study are shown in Table 1, along with the percentage increases from the respective steady-state limits. The extinction values for χ_{max} in unsteady flames range from 1.85 to 2.215 s^{-1} and are higher only by 45 to 73% than the limit obtained in steady-state flames (1.28 s^{-1}). Among all of the characterizing variables, χ_{stoich} most nearly represents the unsteady extinction process, with only a variation of 30 to 53% from the steady-state limit.

3.10. Unified characterization of extinction in unsteady flames

The fact that the scalar dissipation rate describes unsteady flame extinction more closely than the strain rate can be understood by considering the chemical and flow nonequilibrium processes that develop in these flames. As the strain rate on the flame is increased, through diffusion, increasingly more reactants are transported into the reaction zone. At lower strain rates, the chemical kinetics can consume all of the entering reactants. However, at higher rates of strain, the chemistry cannot cope with the large reactant fluxes and, therefore, flame cooling occurs. As discussed previously, the strain rate represents reactant fluxes transported into the reaction zone only in the case of steady-state flames. When flow nonequilibrium occurs, the strain rate does not take into account the time lag between the diffusion and convection processes and, hence, cannot represent the extinction process. Since the scalar dissipation rate describes the diffusion process, it is less sensitive to the flow nonequilibrium that develops in unsteady flames. However, the scalar dissipation rate can represent the chemical kinetics in the flame zone only

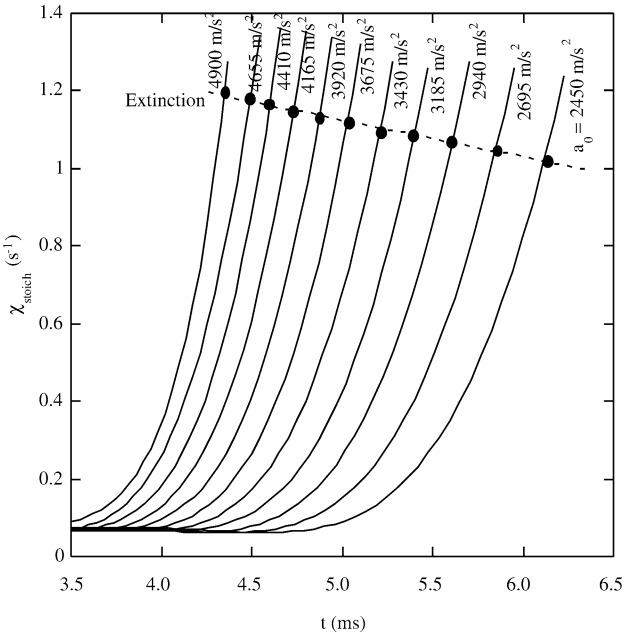

Fig. 23. Variations of the scalar dissipation rate at stoichiometry with time for double-vortex/flame interactions simulated using various rates of increase in injection velocity.

Table 1
Values of various characteristic variables at extinction in unsteady flames

Characteristic variable	Steady-state extinction limit (s^{-1})	Values at extinction in unsteady flames	
		Actual variation (s^{-1})	Percent variation above steady-state limit
k_a	1410	2610–3195	85–127
k_f	1678	3240–4000	93–138
k_{stoich}	2460	5950–7950	142–223
$\chi_{\max}$	1.28	1.85–2.215	45–73
χ_{stoich}	0.78	1.02–1.193	30–53

when the diffusion time scale is far greater than the chemical (reaction) time scale—which exists in unstretched flames where the reactions are limited by the diffusion process. When chemical nonequilibrium occurs (chemistry-limited situation), the scalar dissipation rate does not take into account the time lag between the diffusion and chemical kinetics and, hence, fails to represent the extinction process. Nevertheless, since the scalar-dissipation rate reflects changes in diffusion more accurately than the strain rate, the former describes the unsteady extinction process more accurately.

To represent the unsteady-extinction process uniquely, one must consider a variable that takes into account both the flow- and the chemical-nonequilibrium processes. Since the strain rate or scalar-dissipation rate can be used to estimate the former, a parameter that can be used to estimate the latter is required. If one assumes that no delay exists between chemical kinetics and heat-release rate, then dT_f/dt (rate of decrease in flame temperature) represents the rate of change in chemical kinetics and, in other words, the rate of change in the chemical-nonequilibrium state. Vortices that move more rapidly result in higher dT_f/dt values at extinction, and those that move more slowly result in lower dT_f/dt values. Therefore, by defining a variable that is proportional to the air-side strain rate and inversely proportional to the temperature-decrease rate (dT_f/dt), one can obtain a universal value for identifying the quenching process in unsteady flames.

By considering both the chemical and flow nonequilibrium states of an unsteady flame, a new variable (σ) is defined as the ratio of the strain rate to the rate of change in flame temperature as follows:

$$\sigma = T_\infty \frac{k_a - k_{a0}}{dT_f/dt}. \tag{3}$$

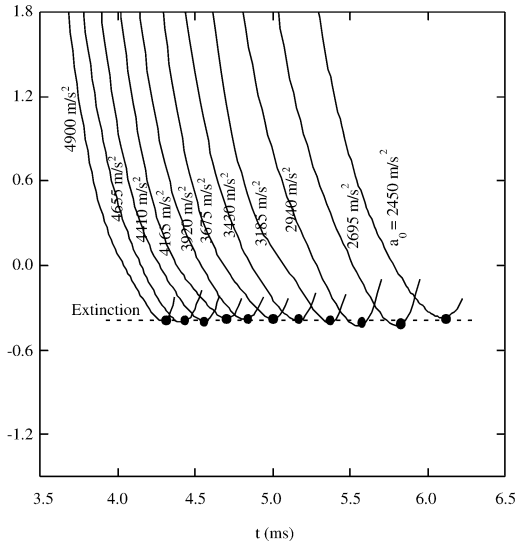

Fig. 24. Variations of the new variable σ with time for double-vortex/flame interactions simulated using various rates of increase in injection velocity.

Here, T_f is the flame (peak) temperature, and k_{a0} is the steady-state air-side extinction strain rate. Values of σ computed at several instants during various vortex/flame interactions are plotted in Fig. 24. In each case as the vortices issued from the fuel and air sides approach the flame surface, σ decreases with interaction time, crosses zero when the instantaneous strain rate reaches the steady-state extinction limit, reaches a minimum value, and then begins to increase. Interestingly, the minimum values of σ for all of the double-vortex/flame-interaction cases are the same—0.39. The striking feature of σ became evident when the extinction condition for each interaction case was plotted in Fig. 24 (filled circles). The extinction conditions coincided with the minima in σ.

The behavior of σ in Fig. 24 can be interpreted as follows: (1) the value of σ at extinction (0.39) is independent of the interaction time scales, and (2) the extinction condition represents the minima in the t-vs-σ profile. The first observation suggests that the new variable σ can be used to characterize the extinction process in unsteady flames—extinction occurs when $\sigma = 0.39$ in any unsteady flame considered in this study. The second observation suggests that extinction in a flame occurs when the behavior of σ with respect to t becomes reversed (changing from decreasing to increasing). Since no extinction criterion was used when plotting variations of σ with respect to t, the natural development of minima at the extinction point suggests that the 1130-K-temperature criterion used in this study for defining the extinction state is fairly accurate. Any extinction criterion based on a flame temperature other than 1130 K would shift the filled circles in Fig. 24 from the minima locations. The values of σ calculated for the double-vortex/flame interactions simulated with different peak-injection velocities (Figs. 13 and 14) are in the range 0.39–0.4. However, σ calculated for the case of the traveling unsteady flame (Fig. 5) is $\sim$0.3, suggesting the need to consider flame movement in the quenching criterion. Interestingly, a variable similar to σ obtained using the scalar dissipation rate in the numerator for representing flow nonequilibrium failed to predict the extinction process of the unsteady flames; in other words, its extinction value depends on the interaction time.

4. Conclusions

Unsteady flames are often studied to gain a better understanding of turbulent-flame structures; such studies facilitate the development of accurate turbulence-chemistry interaction models. An experimental and numerical study has been performed to identify the time-dependent flame structure that develops during an interaction between multiple vortices and the flame surface. A time-dependent model, known as UNICORN, that incorporates 13 species and 74 reactions among the constituent species has been used for the simulation of unsteady flames resulting from multivortex/flame interactions in opposing-flow hydrogen jet diffusion flames. In the past this model has been validated by direct simulation of several steady-state and unsteady axisymmetric counterflow and coflow jet diffusion flames. Phase-locked experiments were conducted, and OH-concentration measurements were made using the PLIF technique.

A steady-state opposing-flow jet flame was first established using the Rolon-burner geometry. Several unsteady flames were then obtained by forcing vortices toward the flame surface from both sides simultaneously using injection tubes placed in the fuel and air nozzles. When the fuel- and air-side vortices were of different sizes, the double-vortex/flame interaction yielded a traveling unsteady flame. The computed flame-extinction process and the propagation of flame edge into the fuel-side vortex compared favorably with the experimental results. To investigate the differences between the steady-state and dynamic extinction processes, stationary unsteady flames were established by forcing equal-sized vortices from the fuel and air nozzles.

It was found that the air-side strain rate, fuel-side strain rate, strain rate at stoichiometric location peak scalar dissipation rate, and scalar dissipation rate at stoichiometric location cannot be used to characterize the quenching process associated with unsteady flames. In general, the extinction values of these vari-

ables in unsteady flames are higher than the respective ones in steady-state flames, and the differences increase with vortex speed. Analysis of flame structures just prior to extinction revealed that dynamic flames encounter flow and chemical nonequilibrium environments. The former arises as a result of the time lag between the diffusion and convection processes, while the latter develops as a result of the time lag between the chemical kinetics and diffusion. Since strain rates represent neither of these nonequilibrium processes, the values of these characteristic parameters at flame extinction are found to vary significantly with vortex/flame interaction time. Even though the scalar dissipation rates represent the flow nonequilibrium accurately, the values of these characteristic parameters at flame extinction also increase with vortex/flame interaction time; however, their variations are much smaller than those observed in strain rates. A new variable (σ) that is proportional to the air-side strain rate and inversely proportional to the rate of change in the flame temperature is proposed to characterize the unsteady extinction process. During a double-vortex/flame interaction, it is found that σ decreases with time, reaches a minimum value at extinction, and then increases again. All of the stationary unsteady flames investigated in the present study were found to be extinguished when the value of σ, independent of the vortex/flame interaction time, reached 0.39. On the other hand, traveling unsteady flames appear to be extinguished at a lower σ value.

Acknowledgments

This work was supported, in part, by the Air Force Office of Scientific Research (Dr. Julian Tishkoff, Technical Monitor). The experimental setup shown in Fig. 1 was designed and built at the Air Force Research Laboratory by Drs. P.H. Renard, J.C. Rolon, and G.J. Fiechtner under a Joint US–French Collaborative Program. The authors acknowledge Marian Whitaker for editorial assistance.

References

[1] R.J. Kee, J.A. Miller, G.H. Evans, G. Dixon-Lewis, Proc. Combust. Inst. 22 (1988) 1479–1486.
[2] G. Dixon-Lewis, Proc. Combust. Inst. 23 (1990) 305–324.
[3] H.K. Chelliah, C.K. Law, T. Ueda, M.D. Smooke, F.A. Williams, Proc. Combust. Inst. 23 (1990) 503–510.
[4] H.C. Hottel, W.R. Hawthorne, Proc. Combust. Inst. 3 (1949) 254–266.
[5] W.M. Roquemore, L.-D. Chen, L.P. Goss, W.F. Lynn, in: R. Borghi, S.N.B. Murthy (Eds.), Turbulent Reactive Flows, in: Lecture Notes in Engineering, vol. 40, Springer-Verlag, Berlin, 1989, p. 49.
[6] N. Darabiha, Combust. Sci. Technol. 86 (1992) 163–181.
[7] F.N. Egolfopoulos, C.S. Campbell, J. Fluid Mech. 318 (1996) 1–29.
[8] H.G. Im, C.K. Law, J.S. Kim, F.A. Williams, Combust. Flame 100 (1995) 21–30.
[9] T.M. Brown, R.W. Pitz, C.J. Sung, Proc. Combust. Inst. 27 (1998) 703–710.
[10] T. Shamim, A. Atreya, Combust. Flame 121 (2000) 59–74.
[11] T. Shamim, A. Atreya, Combust. Flame 123 (2000) 241–251.
[12] A.F. Ghoniem, M.C. Soteriou, B.M. Cetegen, O.M. Kino, Proc. Combust. Inst. 24 (1992) 223–230.
[13] F.N. Egolfopoulos, Int. J. Energy Res. 24 (2000) 989–1010.
[14] B. Cuenot, F.N. Egolfopoulos, T. Poinsot, Combust. Theory Modeling 4 (2000) 77–97.
[15] P.H. Paul, H.N. Najm, Proc. Combust. Inst. 27 (1998) 43–50.
[16] G. Patnaik, K. Kailasanath, Proc. Combust. Inst. 27 (1998) 711–717.
[17] W.T. Ashurst, Combust. Sci. Technol. 92 (1993) 87–103.
[18] V.S. Santoro, D.C. Kyritsis, A. Linan, A. Gomez, Proc. Combust. Inst. 28 (2000) 2109–2116.
[19] W.L. Roberts, J.F. Driscoll, M.C. Drake, J.W. Ratcliffe, Proc. Combust. Inst. 24 (1992) 169–176.
[20] J.C. Rolon, F. Aguerre, S. Candel, Combust. Flame 100 (1995) 422–429.
[21] P.H. Renard, D. Thevenin, J.C. Rolon, S. Candel, Prog. Energy Combust. Sci. 26 (2000) 225–282.
[22] D. Tevenin, P.H. Renard, G.J. Fiechtner, J.R. Gord, J.C. Rolon, Proc. Combust. Inst. 28 (2000) 2101–2108.
[23] V.R. Katta, W.M. Roquemore, Proc. Combust. Inst. 28 (2000) 2055–2062.
[24] V.R. Katta, C.D. Carter, G.J. Fiechtner, W.M. Roquemore, J.R. Gord, J.C. Rolon, Proc. Combust. Inst. 27 (1998) 587–594.
[25] K. Yoshida, T. Takagi, Proc. Combust. Inst. 27 (1998) 685–692.
[26] V.R. Katta, T.R. Meyer, J.R. Gord, W.M. Roquemore, Combust. Flame 132 (2003) 639–651.
[27] T. Poinsot, A. Trouve, D. Veynante, S. Candel, E. Esposito, J. Fluid Mech. 177 (1987) 265.
[28] D. Thevenin, P.H. Renard, J.C. Rolon, S. Candel, Proc. Combust. Inst. 26 (1996) 1079–1086.
[29] M.D. Smooke, A. Ern, M.A. Tanoff, B.A. Valdati, R.K. Mohammed, D.F. Marran, M.B. Long, Proc. Combust. Inst. 26 (1996) 2161–2168.
[30] V.R. Katta, W.M. Roquemore, AIAA J. 36 (11) (1998) 2044–2054.
[31] V.R. Katta, W.M. Roquemore, Calculation of premixed methane–air flame using detailed chemical kinetics, in: Proceedings of the 1998 Technical Meeting of the Central States Section of the Combustion Institute, The Combustion Institute, Pittsburgh, PA, 1998.
[32] W.M. Roquemore, V.R. Katta, J. Visualization 2 (3/4) (2000) 257–272.
[33] M. Frenklach, H. Wang, M. Goldenberg, G.P. Smith, D.M. Golden, C.T. Bowman, R.K. Hanson, W.C. Gardiner, V. Lissianski, Gas Research Institute Techni-

cal Report No. GRI-95/0058, Gas Research Institute, Chicago, November 1, 1995.
[34] B.P. Leonard, Comput. Methods Appl. Mech. Eng. 19 (1) (1979) 59–98.
[35] V.R. Katta, L.P. Goss, W.M. Roquemore, AIAA J. 32 (1) (1994) 84–94.
[36] F. Grisch, B. Attal-Tretout, P. Bouchardy, V.R. Katta, W.M. Roquemore, J. Nonlinear Opt. Phys. Mater. 5 (3) (1996) 505–526.
[37] J. Warnatz, U. Maas, R.W. Dibble, Combustion, Physical and Chemical Fundamentals, Modeling and Simulation, Experiments, Pollutant Formation, Springer-Verlag, Heidelberg, 1996, p. 127.
[38] R.W. Bilger, Turbulent flows with nonpremixed reactants, in: P.A. Libby, F.A. Williams (Eds.), Turbulent Reacting Flows, in: Topics in Applied Physics, vol. 44, Springer-Verlag, New York, 1980, p. 65.
[39] R.W. Bilger, Proc. Combust. Inst. 22 (1988) 475–488.
[40] E. Gutheil, G. Balakrishnan, F.A. Williams, in: N. Peters, B. Rogg (Eds.), Lecture Notes in Physics, Springer-Verlag, New York, 1993, p. 177.
[41] G.T. Fiechtner, P.H. Renard, C.D. Carter, J.R. Gord, J.C. Rolon, J. Visualization 2 (2000) 331–342.
[42] G.T. Fiechtner, C.D. Carter, K.D. Grinstead, J.R. Gord, W.M. Roquemore, J.C. Rolon, Flame–vortex interactions in a non-premixed H_2/N_2/air counterflow burner, in: 34th AIAA/ASME/SAE/ASEE Joint Propulsion Conference & Exhibit, Cleveland, OH, 1998, AIAA 98-3770.
[43] R.S. Sheinson, J.E. Penner-Hahn, D. Indritz, Fire Safety J. 15 (1989) 437–450.
[44] A.F. Roberts, B.W. Quince, Combust. Flame 20 (1973) 245–251.
[45] D.C. Kyritsis, V.S. Santoro, A. Gomez, Measurements and computations of scalar dissipation rate in vortex perturbed counterflow diffusion flame, in: Proceedings of the 2001 Technical Meeting of the Eastern States Section of the Combustion Institute, The Combustion Institute, Hilton Head, SC, 2001, pp. 320–323.
[46] F. Takahashi, V.R. Katta, J. Propulsion Power 11 (1) (1995) 170–177.